POLITECNICO DI TORINO
Repository ISTITUZIONALE

Topological optimization of 3DP claddings for indoor moisture buffering

Original
Topological optimization of 3DP claddings for indoor moisture buffering / Gentile, V., Vargas Juan, Diego., Autretto, G., Serra, V., Fantucci, S.. - In: BUILDING SIMULATION CONFERENCE PROCEEDINGS. - ISSN 2522-2708. - ELETTRONICO. - 19:(2025). (Building Simulation 2025: 19th Conference of IBPSA Brisbane (AUS) Aug 24-27, 2025) [10.26868/25222708.2025.1711].

Availability:
This version is available at: 11583/3011787 since: 2026-06-27T17:40:39Z

Publisher:
International Building Performance Simulation Association (IBPSA)

Published
DOI:10.26868/25222708.2025.1711

Terms of use:

This article is made available under terms and conditions as specified in the corresponding bibliographic description in the repository

Publisher copyright

(Article begins on next page)

19 November 2026

BUILDING SIMULATION 2025 24–27 AUG BRISBANE CARBON AND CLIMATE RESPONSIVE

International Building Performance Simulation Association

Topological optimization of 3DP claddings for indoor moisture buffering

Vincenzo Gentile[1], Juan Diego Vargas Velasquez[1], Giorgia Autretto[1], Valentina Serra[1], Stefano Fantucci[1]
[1] Department of Energy, Politecnico di Torino, Turin, Italy
vincenzo.gentile@polito.it

Abstract

Using 3DP building components as indoor passive humidity regulators can enhance indoor environmental quality while reducing energy usage for active ventilation and air conditioning. This study optimizes the Moisture Buffering Value (MBV) of highly hygroscopic 3DP claddings, focusing on design approaches that increase *surface area* for moisture transfer. Although chemical additives boost MBV, effectiveness is restricted by limited wall area available and shallow penetration depth. Components with complex geometries fabricated via Liquid Deposition Modeling (LDM) offer extended surfaces to enhance *mass transfer*. This study implemented a multi-platform workflow in Python and Grasshopper for modifying morphological features of 3DP components with *Triply Periodic Minimal Surfaces* (TPMS) lattices to improve total moisture transfer.

Key Innovations

- Workflow partially implemented within Grasshopper, enabling efficient morphological characterization, component-scale and room-scale simulations of 3D-printed plaster components.
- Innovative use of Triply Periodic Minimal Surfaces (TPMS) to enhance moisture buffering through increased surface area.

Practical Implications

This paper contributes to passive indoor humidity regulation, enhancing occupant comfort while reducing reliance on active HVAC systems. Additionally, it shows architects and practitioners a flexible and scalable assessment methodology to optimize building components for improved moisture control.

Introduction

Indoor environmental quality and moisture buffering

Relative humidity (RH%) plays a key role in thermal comfort and occupants' health. Excessively high or low RH can cause discomfort, health issues, promotion of biological growth, and increased energy consumption for active climate control (Schweiker et al., 2020). A promising passive strategy to regulate indoor RH involves hygroscopic properties of interior walls and ceilings. When these surfaces exhibit a high moisture buffering value (MBV), hence above 3 g/m² %RH, they can absorb and release moisture in response to fluctuations in ambient humidity (Gentile, Vargas Velasquez, et al., 2024). To enhance MBV, conventional approaches modify material composition through chemical additives or high-porosity aggregates (Gentile et al., 2023; Mnasri et al., 2020; Zu et al., 2020). While these methods can achieve MBV values between 6 and 15 g/(m²·%RH) (Gentile, Vargas Velasquez, et al., 2024), their effectiveness is constrained by the limited flat surface of interior partitions. Additionally, even though the effective penetration depth varies depending on material characteristics, for daily moisture fluctuations it is typically less than a few millimetres, meaning thicker material layers do not necessarily improve proportionally buffering performances (Cascione et al., 2020). This limitation underscores the importance of optimizing material usage to balance efficiency, environmental impact, and cost-effectiveness.

Opportunities offered by advanced manufacturing

Additive manufacturing is increasingly adopted in construction, offering new approaches for mass customization and design flexibility (Paoletti, 2017). Liquid Deposition Modeling (LDM) is particularly suitable for clay- and mortar-based materials, as their viscous consistency allows extrusion through a nozzle to create complex 3D geometries (Rael & San Fratello, 2016). This technique enables the integration of macro-level features that enhance functional properties like moisture buffering and heat transfer (Briels et al., 2022; Gentile, Vargas Velasquez, et al., 2024; Piccioni et al., 2023; Posani et al., 2025).

LDM facilitates the fabrication of geometrically complex plaster-based components, including textured surfaces, lattice scaffolds, and channels that increase total surface (Altıparmak et al., 2022). These topological features can be strategically placed to maximize the rates of moisture mass transfer (Schiavi et al., 2024) without compromising mechanical integrity. However, increasing specific surface area (m^2/m^3) also leads to higher pore tortuosity (the ratio of the actual air path length within the pores to the scaffold thickness) (Schiavi et al., 2022). Greater pore tortuosity acts as a barrier to the natural air circulation within the component structure, reducing vapor supply to internal regions to a flat surface, where all points are equally exposed to bulk room humidity. Thus, optimizing airflow topology is crucial in the design of 3D-printed components to maximize moisture buffering performance.

https://doi.org/10.26868/25222708.2025.1711

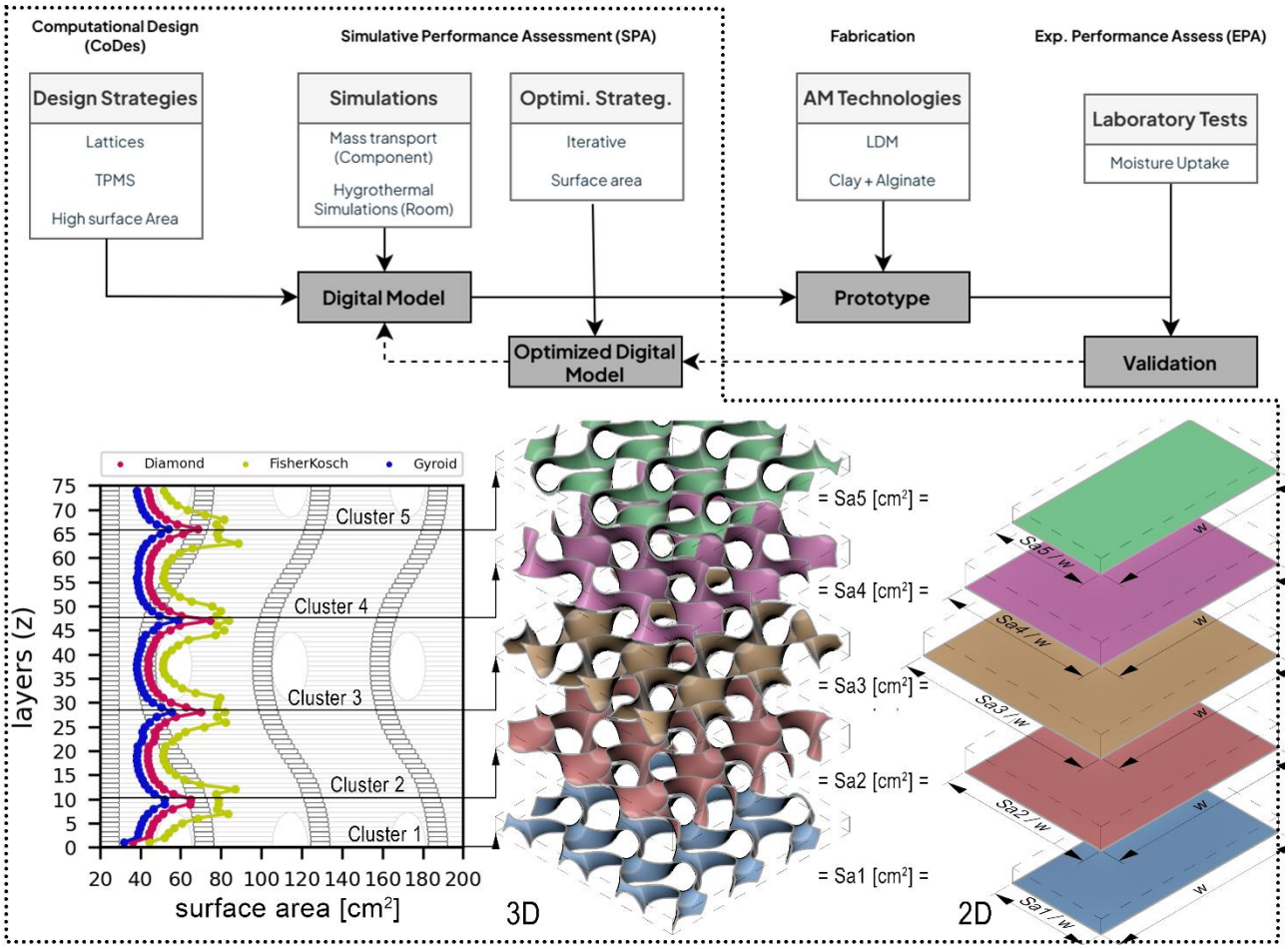


Figure 1 – Methodology - Workflow overview & Component scale characterization.

Initially developed for mechanical and aerospace engineering, topology optimization has gained traction in architecture and building engineering. It employs computational algorithms (e.g., biomimicry, generative design) to develop structures with high mechanical performance and minimal material usage (Vincent, 2001).

Lattice structures like the Triply Periodic Minimal Surfaces (TPMS) are popular approaches for creating components with substantial surface area for mass and heat transfer (Feng et al., 2022). These kinds of structures have even been found in biological structures (Gan et al., 2016).

Research objectives and contributions

This research does not employ traditional topology optimization algorithms, which typically optimize material distribution within a defined design domain to enhance mechanical performance. Instead, it focuses on morphological optimization of 3D-printed clay-based components fabricated through Liquid Deposition Modeling (LDM). By systematically varying *global topological* features such as *TPMS configurations*, *voxel arrays*, and *porosity*, this approach enhances moisture absorption performance in a controlled and predictable manner, without relying on complex computational topology optimization methods.

The primary objective is to develop an integrated simulation workflow that links parametric design and optimization of 3D-printed mortar geometries, which in future development will integrate with building-level simulations. Current specific goals are:

1. Identify optimal morphological properties such as *porosity* and *surface area* to maximize MBV.
2. Evaluate and compare the moisture buffering capacities of selected TPMS configurations.

Methodology

Research framework overview

This study explores the potential of applying TPMS to 3D printed building components acting as passive moisture regulators. To assess the components' moisture buffering properties, the implemented methodology leveraged computational design tools such as Grasshopper for Rhinoceros, which was used to generate, characterize, assess and manufacture the samples. **Figure 1** illustrates the workflow integrating design and analysis with component-scale and room-scale simulations. The process begins with algorithmic modelling and morphological characterization of the components with TPMS infills, followed by moisture transport simulations at the component scale, using Fick's law.

As shown in **Figure 1** the proposed *Design for Additive Manufacturing (DfAM)* (Leschok et al., 2023) methodology integrates four main stages: *Computational Design* (CoDes), *Simulative Performance Assessment*

https://doi.org/10.26868/25222708.2025.1711

(SPA), *Fabrication*, and *Experimental Performance Assessment* (EPA). Initially, *design strategies*—such as TPMS lattice structures—are defined and modelled digitally. These models undergo iterative optimization through simulations at the focusing on maximizing moisture buffering performance. To this end, a Python based plugin that solves dynamically the moisture diffusion through the material, based on Fick's law, has been developed within Grasshopper's environment.

Geometrical Characterization of TPMS

The selected TPMS were Gyroid, Diamond, and Fisher-Koch S (FK), widely studied in recent literature (Feng et al., 2022). These lattices were digitally generated using plugins such as Axolotl (Bernhard et al., 2020) and Isopod, forming single-walled, orthogonal lattice arrangements of 150x150x75 mm, designed specifically for additive manufacturing without adjacent extrusions (Agrawal & Mukherjee, 2022). To accurately characterize morphological aspects—including *surface area (Sa), volume of printed solid (Vsol) and of empty portion (Vair), porosity (ε)* and *tortuosity (τ),* the calculations were based directly on the 3D printing path rather than the volumetric digital model (Gentile et al., 2024). This method proved more reliable, as it better represented the actual morphological features of single-walled 3D-printed components (Zohdi & Yang, 2021).

Figure 1 illustrates these single-walled components alongside a plot comparing the calculated *surface area* per layer (in cm²) for a 3x3x1 voxel array configuration across *Diamond, Gyroid,* and *FK* structures. It also demonstrates the approach used to reinterpret the complex 3D geometries as simplified 2-dimensional surfaces used in the component-scale moisture transport simulations. For enhanced simulation precision, the samples were discretized along the z-axis into five clusters (*C1-C5*), that were characterized separately. Then the clusters' morphological properties, such as *surface area* (Sa_1–Sa_5) were computed, and the equivalent 2D representations were derived from the ratio Sa / w, where w is one of the two dimensions that represent the geometrical section of the extruded filament.

Table 1 - Surface area calculations

TPMS	Min Sa. [cm²]	Max Sa. [cm²]
Diamond	2999	7136
Gyroid	2590	5930
FK	3837	9667

Optimization parameters: Incidence of voxel arrays, surface area, porosity, tortuosity

The optimization strategy consisted of maximizing *surface area* varying only the samples' (x,y,z) voxel arrays, while calculating their morphological properties, summarized in **Figures 2 -3** and **Table 1**. All the possible solutions within the design space *(thirty-six)* were iteratively generated.

The arrays ranged from 2x2x1 to 7x7x2, where x and y were always equal.

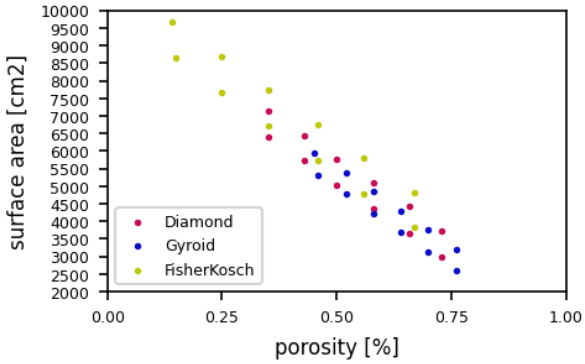


Figure 2 - Surface area [cm²] and porosity [ε].

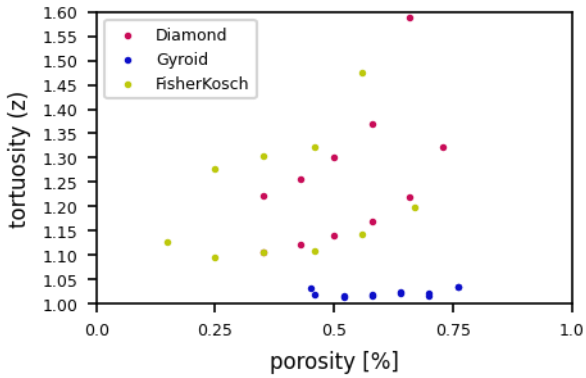


Figure 3 – Tortuosity [τ] and porosity [ε] per sample.

For example, **Figure 6** displays the digital model and 3DP prototype of a 3x3x1 Gyroid array. Even though the main objective was to maximize components' *surface area* due to its incidence on MBV (Vargas et al., 2023), *porosity* and *tortuosity* should also be considered. Studies about *permeability* in TPMS lattices, like *(Guerreiro et al., 2020)* show a direct and almost linear relationship between *permeability* and *porosity*. Others, like (Santos et al., 2020), found that in Darcian regime, *tortuosity* affected *permeability* in TPMS arrays with equivalent *porosity,* as arrays with higher *tortuosity* showed lower discharge coefficient.

Simulation

The simulation approach is schematized in **Figure 4a,** illustrating the cluster-based method used to discretize the TPMS structures. The sample is divided into *j* clusters along (*z*), each containing a solid and void zone. Despite the periodic geometric nature of the TPMS, the morphological characteristics of these clusters can vary depending on their position along the z-axis, necessitating individual characterization for accurate simulations.

Moisture exchange occurs between the TPMS clusters and the *Room Bulk Volume* (RBV), while internal recirculation within each cluster depends on the TPMS topology and the z-layer position (**Figure 4b**). This method allows differentiation of moisture exchange potential across clusters based on the z-coordinates and specific *Air Change Rate* (ACH) values relative to the RBV. Consequently, local RH and T conditions within each empty zone evolve dynamically, affecting the moisture transfer rate.

https://doi.org/10.26868/25222708.2025.1711

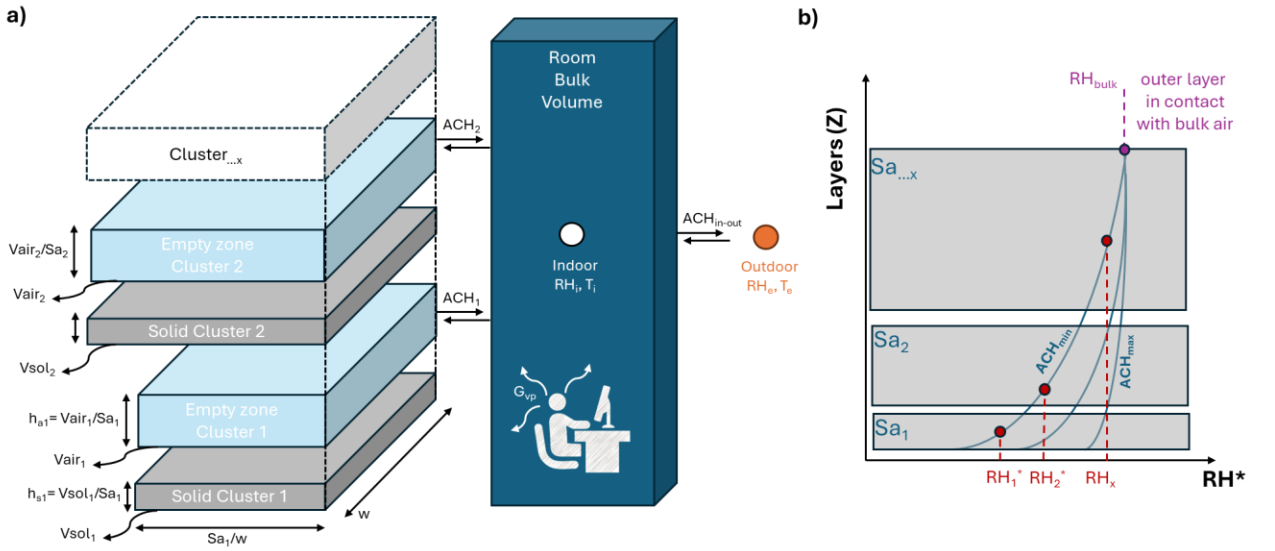


Figure 4 – Simulation methodology for the mass transport through the 3DP panel and exchange with surrounding air.

The moisture transfer through the solid sorbent within each cluster follows the *Fickian diffusion model* described in eq. (1). At each time step, eq. (1) is solved for every solid cluster within the TPMS. The initial moisture concentration across the material thickness and the equilibrium moisture content at the air/material interface (Wt_{eq}) are defined as boundary conditions. The material is assumed to reach instantaneous equilibrium at the interface, where the Wt_{eq} is determined every time by the RH occurring in the empty zone of each cluster.

$$\frac{For\ each}{cluster\ j}\begin{cases}\dfrac{\partial w_t(x,t)}{\partial t}_j = \dfrac{\partial}{\partial x}\left[D(w_t)\cdot\dfrac{\partial w_t(x,t)}{\partial x}\right]_j \\ \left.\dfrac{\partial w_t(x,t)}{\partial x}\right|_{x=0,t_j} = 0 \\ w_t(x=+s,t)_j = W_{t_{eq_{j_{(t-1)}}}} \\ w_t(x,t=0)_j = w_{t_0}\end{cases} \quad (1)$$

Eq. (2) calculates the moisture flux adsorbed or released from each cluster's surface *j*.

$$G_{BUF_j} = \frac{\partial w_t}{\partial t}_j S_{a_j} * h_{sjj} * \rho_d = \frac{\partial w_t}{\partial t}_j * V_{sol\,j} * \rho_d \quad (2)$$

Since $Wt_{eq(t-1)}$ changes over time, the system requires the solving the mass balance equation reported in eq. (3) for each empty zone, where P_v denotes water vapor partial pressure. Here, the buffering mass flux (G_{BUF_j}) is balanced with the moisture content in the empty zone and the mass transfer between the RBV and cluster j, regulated by ACH_j. As shown in **Figure 2 and 3**, there is an inverse correlation between *exposed surface area* and *porosity*. Consequently, as the ratio of *exposed surface area* per *volume unit* ($S_{a_j}/V_{air\,j}$) and *tortuosity* rise, the harder the interaction between component and RBV will be. This phenomenon is especially relevant in the deeper layers of the TPMS as *air velocity* drops (**Figure 4b**). Hence the Sa_1 respect to the $Sa_{...x}$, will equilibrate with a RH_1^* that is lower than the RH_x^* (which is the closest value respect to the bulk condition RH_{bulk}=RH_i).

$$\frac{V_{air_j}}{R_v T_j}\frac{\partial P_{v_j}}{\partial t} = \frac{\left(P_{v_j} - P_{v_i}\right) ACH_j * V_{air\,j}}{3600\ R_v T_i} - G_{BUF_j} \quad (3)$$

For simplicity, thermal equilibrium is assumed between the cluster and the RBV (hence T_j=T_i).

Finally, summing the mass transfer across all the TPMS clusters balances with the RBV moisture balance which accounts for: *i*) the internal moisture generation from human occupants; *ii*) the moisture exchange with outdoor air (which has air conditions T_e and RH_e) happening at the rate $ACH_{in\text{-}out}$. Eq. (4) reports this mass balance:

$$\frac{V_{RBV}}{R_v T_i}\frac{\partial P_{v_i}}{\partial t} = \frac{\left(P_{v_i} - P_{v_e}\right) ACH_{in-out} V_{air\,RBV}}{3600\ R_v T_i} + G_{vp} \ldots \\ \ldots - \sum G_{BUF_j} \quad (4)$$

For simplicity, the indoor and outdoor temperatures are assumed equal (T_i=T_e), while the outdoor RH is constant but different from the indoor value ($Pv_i \neq Pv_e$). The internal moisture generation (G_{vp}) is linked to the metabolic activity of occupants (LHG) and the number of occupants (n), as in eq. (5).

$$G_{vp} = \frac{LHG}{2500} * \frac{n}{1000} \quad (5)$$

Materials

The TPMS component is made from an enhanced mortar, incorporating Alginate hydrogel, which increases moisture capacity by 10 times compared to conventional limestone plaster (Gentile et al., 2023). The moisture adsorption isotherm follows eq. (6), where Figure 5 illustrated its behaviour at 23°C. This double-entry function accounts for temperature variations, allowing for non-isothermal studies.

Another critical property is the internal resistance to moisture diffusion within the solid TPMS structure. Eq.

https://doi.org/10.26868/25222708.2025.1711

(7) describes the moisture diffusivity as a function of temperature and water content.

For isothermal conditions, diffusivity is mainly influenced by c_0. The coefficients were derived from dynamic tests (Gentile, Calò, et al., 2024).

$$w_{t_{eq}} = \begin{pmatrix} d_0RH^3 + \\ d_1RH^2 + \\ d_2RH + \\ d_3 \end{pmatrix} * \begin{pmatrix} d_4T^3 + \\ d_5T^2 + \\ d_6T + \\ d_7 \end{pmatrix} \quad (6)$$

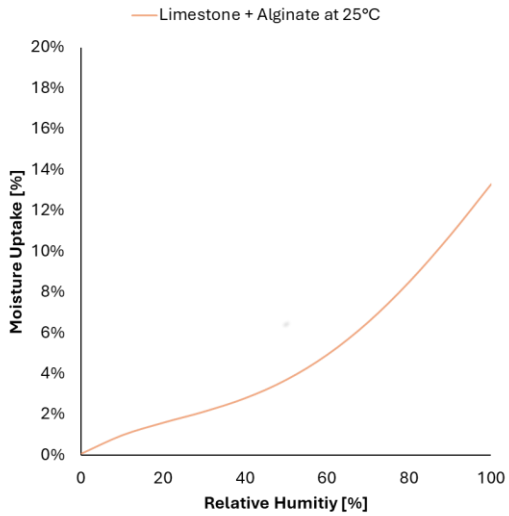


Figure 5 - Printed material adsorption isotherm at 25°C.

$$D_{w_t,T} = c_0 + c_1T + c_2w_t^{-\frac{E_a c_4}{T}} \quad (7)$$

Because this case study considers an isothermal condition, the diffusivity coefficient is prominently influenced by coefficients c0. The coefficients are fitted from the dynamic tests reported in (Gentile et al., 2023).

Fabrication

An example of the 3DP prototypes manufactured with LDM using a Delta WASP 40100 with a nozzle of 2mm, layer height of 1mm and layer thickness of ~4mm at a speed of 7000mm/min is reported in **Figure 6**. The components were fabricated using single-wall extrusion as it drastically minimizes printing time despite reducing object resolution and detail level.

Sangiorgio et al., 2022 used the same 3D printing setup (3D printer, nozzle and layer height), differing only in printing speed (1800mm/min), to manufacture clay components with TPMS infills with a *gross volume* of 1687.5 [cm^3], equivalent to the *gross volume* of this study's samples. The average manufacturing time of their components was 180 min, that at a speed of 7000 mm/min would have been of ~46 min. Conversely, the average of the calculated manufacturing time per sample of this study was ~26 min, representing a 44% reduction in printing time.

Case study: Simulated room subjected to square-wave occupancy pattern

The simulated room has a dimension of 3x4x3 m, and accommodates 4 occupants, each performing light activities (LHG=75W). The study evaluates the moisture buffering capacity of the TPMS component under a square-wave occupancy schedule that takes inspiration from the NORDTEST protocol used for the evaluation of the MBV of materials and components. Specifically, during 24 hours of test, the room is fully occupied for the first 8 hours, followed by 16 hours of vacancy. The initial moisture distribution within the material is homogeneous and in equilibrium with indoor air at 50% RH and 23°C. Indoor air temperature remains constant at 23°C, while outdoor conditions are also 23°C with 50% RH, maintained throughout the 24-hour testing period. The results of the simulation are presented in the following section.

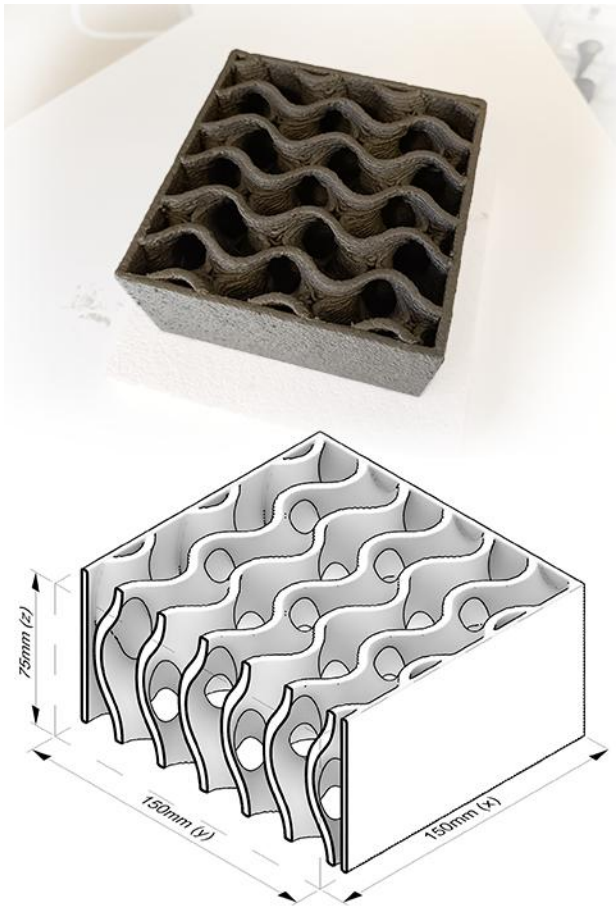


Figure 6 - Gyroid 3x3x1 array. 3DP prototype (Top), digital model (Bottom).

Results

The *specific surface area*, defined as the surface area available for moisture interaction per unit of volume (m²/m³), varied significantly across the studied TPMS types *(Diamond, Gyroid, and Fisher-Koch S).* As summarized in **Table 2**, the *Fisher-Koch S* structure demonstrated the highest specific surface area range (2.4–6.0 m²/m³), followed by the *Diamond* (1.9–4.5 m²/m³) and *Gyroid* (1.6–3.7 m²/m³) configurations. **Figure 7** illustrates the relationship between specific surface area and porosity for each TPMS design. A clear inverse

https://doi.org/10.26868/25222708.2025.1711

correlation is observed: as porosity increases, the specific surface area decreases across all structures. Notably, *Fisher-Koch S* configurations consistently achieve higher specific surface areas at equivalent porosity levels compared to Diamond and Gyroid structures, indicating a potential advantage of the Fisher-Koch S TPMS for moisture buffering due to its superior surface-to-volume ratio.

Table 2 – Specific surface area.

TPMS	Min Sa. [m^2/m^3]	Max Sa. [m^2/m^3]
Diamond	1.9	4.5
Gyroid	1.6	3.7
FK	2.4	6.0

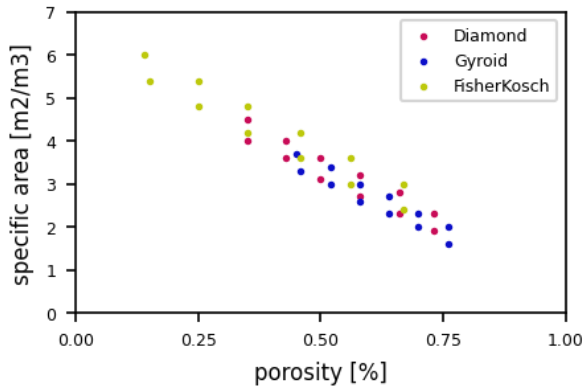


Figure 7 - Specific area [cm2/cm3] and porosity [ε].

The simulation model described in the Methodology was applied to the reference case study to evaluate how variations in specific surface area (A/V) affect moisture transport, particularly water vapor pressure, within both the TPMS structure (**Figure 8**) and the RBV (**Figure 9**). **Figure 8a** presents the average internal vapor pressure (Pv_j) inside the TPMS as a function of A/V (x-axis, m^2/m^3) over the moisture-loading cycle (y-axis, hours). The initial P_vi corresponds to the reference conditions (T_i = 23°C, RH_i = 50%) and is approximately 1.4 kPa.

At low A/V ratios, Pv_j increases rapidly due to moisture released from internal loads into the RBV. However, when A/V exceeds 1 m^2/m^3, Pv_j remains close to its initial value, indicating that the high surface area enhances moisture absorption capacity. Beyond A/V = 1.5 m^2/m^3, the maximum vapor pressure in the TPMS stays below 1.5 kPa (**Figure 8a**), showing minimal changes up to 3.5 m^2/m^3, even when the internal air change rate (ACH_j) increases to 1 h^{-1}. These findings suggest that further increasing A/V beyond 1.5–3.5 m^2/m^3 may complicate manufacturing without yielding significant improvements in moisture buffering. However, this conclusion is specific to the tested case study and will vary based on room size, material properties, and indoor/outdoor environmental conditions.

This simulation tool can be used to determine the required number of panels needed, or the surface to be covered, to achieve a desired moisture buffering effect in a room. **Figure 9** illustrates how the vapor pressure in the Room Bulk Volume (RBV) varies with the total installed panel surface area.

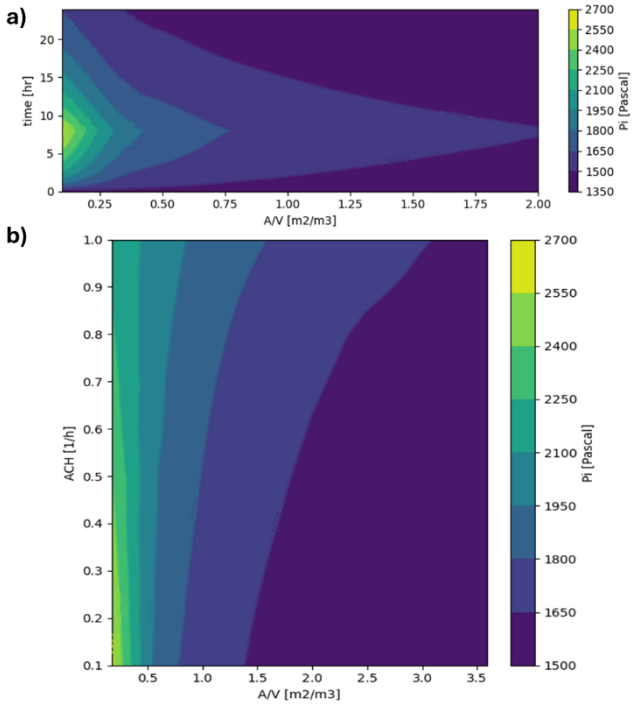


Figure 8 - a) water vapor pressure during time within the TPMS with ACHj=1 h^{-1}. b) maximum vapor pressure within the TPMS at different ACHj.

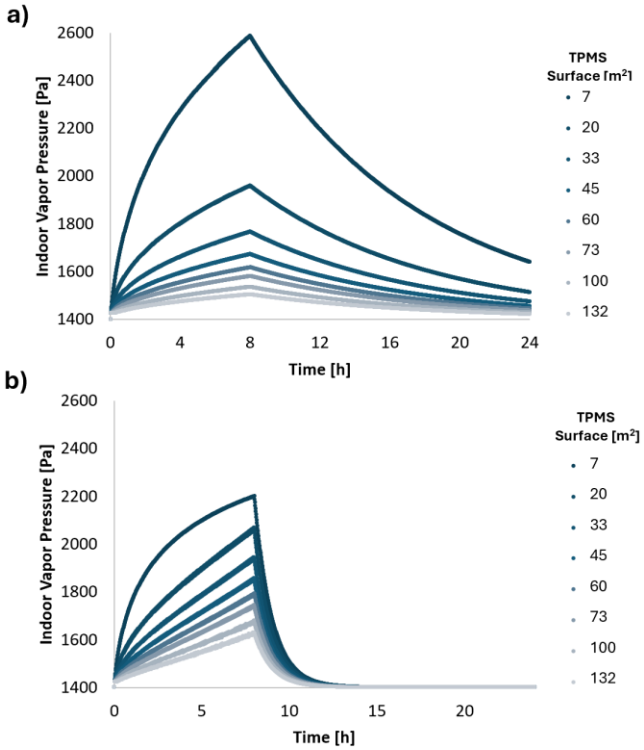


Figure 9 - Influence on the indoor Pv of the RBV at different TPMS surfaces with ACH=0.1h^{-1} in a) and ACH=1h^{-1} in b).

The 3D-printed panel shown in **Figure 6** has a gross volume of 0.15 × 0.15 × 0.075 m and a total surface area of 0.3 m^2, significantly larger than its cross-sectional area

https://doi.org/10.26868/25222708.2025.1711

of only 0.0225 m². The simulated surface areas of 7, 20, 33, 45, 60, 73, 100, and 132 m² correspond to 23 to 440 printed modules, which in terms of occupied wall surface range from 0.52 to 9.9 m². At the highest tested surface area (132 m²), the vapor pressure (Pv_i) stabilizes, showing fluctuations of less than 100 Pa over time. This effect is only achievable due to the intricate geometry of the TPMS. To reach the same effective surface area using conventional flat walls, one would require 132 m², which exceeds the maximum available wall and ceiling surface area (66 m²) in the tested room. In contrast, TPMS panels achieve this performance while occupying just 10 m² of vertical wall space, highlighting their efficiency in optimizing moisture buffering.

Conclusion

This study shows that 3D-printed panels with complex geometries can enhance moisture buffering in indoor environments, mitigating fluctuations of relative humidity induced by occupancy. By parametrically generating Triply Periodic Minimal Surfaces (TPMS) such as Fisher-Koch, Gyroid, and Diamond, and systematically varying voxel arrays, it was possible to achieve large increases in effective surface area per unit volume. The simulation methodology makes it possible to identify the threshold of total surface area of TPMS component, required to obtain consistent moisture buffering in a room. Results specific to the tested case study demonstrated that beyond approximately 1.5–3.5 m²/m³, further increases in specific surface area provide only marginal moisture-buffering gains. However, this finding is case-specific, highlighting the importance of tailoring morphological optimizations always considering as input for the modelling the room size, occupant load, ventilation regimes, and material properties. A key-outcome of this research is the confirmation that 3D printing enables significantly more total surface area than what is achievable with flat panels alone. As illustrated, up to 132 m² of moisture-active surface could be installed on just 10 m² of wall space using these topologies, an approach impossible with standard flat plasters. Moreover, the cluster-based simulation method allowed each "slice" of the 3D-printed component to be treated according to its unique geometry, airflow characteristics, and moisture exchange potential. This level of detail fosters more accurate predictions of localized vapor distribution and overall buffering performance. Beyond its immediate practical value for improved indoor humidity control and occupant comfort, this work shows the potential of integrating advanced manufacturing methods with computational optimization. At the present time, the simulation tool has been partially integrated within Grasshopper. Future developments aim at fully integrating it, generating a seamless *DfAM* workflow to assess moisture buffering at component and building scales. Future studies may as well extend the model to account for non-isothermal conditions, different material blends, or multiscale heterogenous topologies. Additionally, further investigation is needed to assess the long-term mechanical durability of 3D-printed components under cyclical humidity exposure. Ultimately, the methodology and results presented here pave the way for designing customizable, high-performance building components that reduce reliance on active HVAC systems and offer passive indoor climate regulation.

Acknowledgement

This study was possible thanks to the Project "Choisis-Characterization of Innovative and Sustainable Insulating Solutions", funded within the Italian National Recovery and Resilience Plan (PNRR), Mission 4 – Education and Research-Measure M4C2 – Investment 1.1 PRIN – Research programs of national interest – project code 2022372TM9, CUP F53D23001540006. The research activity presented in this paper is done in a project funded under the National Recovery and Resilience Plan (NRRP), Mission 4 Component 2 Investment 1.3 - Call for tender No. 1561 of 11.10.2022 of Ministero dell'Università e della Ricerca (MUR); funded by the European Union – NextGenerationEU. Award Number: Project code PE0000021, Concession Decree No. 1561 of 11.10.2022 adopted by Ministero dell'Università e della Ricerca (MUR), CUP E13C22001890001, according to attachment E of Decree No. 1561/2022, Project title "Network 4 Energy Sustainable Transition – NEST".

References

Agrawal, A., & Mukherjee, S. (2022). 3D printing of single-walled objects. *Materials Today: Proceedings*, *66*, 3743–3747. https://doi.org/10.1016/j.matpr.2022.06.006

Altıparmak, S. C., Yardley, V. A., Shi, Z., & Lin, J. (2022). Extrusion-based additive manufacturing technologies: State of the art and future perspectives. In *Journal of Manufacturing Processes* (Vol. 83, pp. 607–636). Elsevier Ltd. https://doi.org/10.1016/j.jmapro.2022.09.032

Briels, D., Kollmannsberger, S., Leithner, F., Matthäus, C., Nouman, A. S., Oztoprak, O., & Rank, E. (2022). Thermal Optimization of Additively Manufactured Lightweight Concrete Wall Elements with Internal Cellular Structure through Simulations and Measurements. *Buildings*, *12*(7). https://doi.org/10.3390/buildings12071023

Cascione, V., Hagentoft, C. E., Maskell, D., Shea, A., & Walker, P. (2020). Moisture buffering in surface materials due to simultaneous varying relative humidity and temperatures: Experimental validation of new analytical formulas. *Applied Sciences (Switzerland)*, *10*(21), 1–22. https://doi.org/10.3390/app10217665

Feng, J., Fu, J., Yao, X., & He, Y. (2022). Triply periodic minimal surface (TPMS) porous structures: From multi-scale design, precise additive manufacturing to multidisciplinary applications. In *International Journal of Extreme Manufacturing* (Vol. 4, Issue 2). IOP Publishing Ltd. https://doi.org/10.1088/2631-7990/ac5be6

Gan, Z., Turner, M. D., & Gu, M. (2016). Biomimetic gyroid nanostructures exceeding their natural origins. *Science Advances*, *2*(5). https://doi.org/10.1126/sciadv.1600084

Gentile, V., Calò, M., Bozlar, M., Simonetti, M., & Meggers, F. (2024). Water vapor mass transfer in

alginate–graphite bio-based hydrogel for atmospheric water harvesting. *International Journal of Heat and Mass Transfer*, *219*. https://doi.org/10.1016/j.ijheatmasstransfer.2023.124794

Gentile, V., Libralato, M., Fantucci, S., Shtrepi, L., & Autretto, G. (2023). Enhancement of the hygroscopic and acoustic properties of indoor plasters with a Super Adsorbent Calcium Alginate BioPolymer. *Journal of Building Engineering*, *76*. https://doi.org/10.1016/j.jobe.2023.107147

Gentile, V., Vargas Velasquez, J. D., Fantucci, S., Autretto, G., Gabrieli, R., Gianchandani, P. K., Armandi, M., & Baino, F. (2024). 3D-printed clay components with high surface area for passive indoor moisture buffering. *Journal of Building Engineering*, *91*. https://doi.org/10.1016/j.jobe.2024.109631

Guerreiro, R., Pires, T., Guedes, J. M., Fernandes, P. R., & Castro, A. P. G. (2020). On the tortuosity of TPMS scaffolds for tissue engineering. *Symmetry*, *12*(4). https://doi.org/10.3390/SYM12040596

Leschok, M. ;, Cheibas, I. ;, Piccioni, V. ;, Seshadri, B. ;, Schlüter, A. ;, Gramazio, F. ;, Kohler, M. ;, Dillenburger, B., Leschok, M., Cheibas, I., Piccioni, V., Seshadri, B., Schlüter, A., Gramazio, F., & Kohler, M. (2023). *ETH Library 3D printing facades: Design, fabrication, and assessment methods Rights / license: Creative Commons Attribution 4.0 International 3D printing facades: Design, fabrication, and assessment methods*. https://doi.org/10.3929/ethz-b-000611431

Mnasri, F., Bahria, S., Slimani, M. E. A., Lahoucine, O., & El Ganaoui, M. (2020). Building incorporated bio-based materials: Experimental and numerical study. *Journal of Building Engineering*, *28*. https://doi.org/10.1016/j.jobe.2019.101088

Paoletti, I. (2017). Mass Customization with Additive Manufacturing: New Perspectives for Multi Performative Building Components in Architecture. *Procedia Engineering*, *180*, 1150–1159. https://doi.org/10.1016/j.proeng.2017.04.275

Piccioni, V., Leschok, M., Lydon, G., Cheibas, I., Hischier, I., Dillenburger, B., Kohler, M., Gramazio, F., & Schlueter, A. (2023). Printing thermal performance: An experimental exploration of 3DP polymers for facade applications. *IOP Conference Series: Earth and Environmental Science*, *1196*(1). https://doi.org/10.1088/1755-1315/1196/1/012063

Posani, M., Voney, V., Odaglia, P., Du, Y., Komkova, A., Brumaud, C., Dillenburger, B., & Habert, G. (2025). Low-carbon indoor humidity regulation via 3D-printed superhygroscopic building components. *Nature Communications*, *16*(1), 425. https://doi.org/10.1038/s41467-024-54944-1

Rael, R., & San Fratello, V. (2016). *Clay Bodies Crafting the Future with 3D Printing Clay*.

Sangiorgio, V., Parisi, F., Fieni, F., & Parisi, N. (2022). The New Boundaries of 3D-Printed Clay Bricks Design: Printability of Complex Internal Geometries. *Sustainability (Switzerland)*, *14*(2). https://doi.org/10.3390/su14020598

Santos, J., Pires, T., Gouveia, B. P., Castro, A. P. G., & Fernandes, P. R. (2020). On the permeability of TPMS scaffolds. *Journal of the Mechanical Behavior of Biomedical Materials*, *110*. https://doi.org/10.1016/j.jmbbm.2020.103932

Schiavi, A., Fiume, E., Orlygsson, G., Schwentenwein, M., Verné, E., & Baino, F. (2022). High-reliability data processing and calculation of microstructural parameters in hydroxyapatite scaffolds produced by vat photopolymerization. *Journal of the European Ceramic Society*, *42*(13), 6206–6212. https://doi.org/10.1016/j.jeurceramsoc.2022.06.022

Schiavi, A., Gabrieli, R., Orlygsson, G., Schwentenwein, M., Verné, E., & Baino, F. (2024). Assessment of permeability and microstructural parameters via fractal modelling in bioactive glass-derived scaffolds produced by vat photopolymerization. *Journal of the European Ceramic Society*, *44*(7), 4689–4698. https://doi.org/10.1016/j.jeurceramsoc.2024.01.095

Schweiker, M., Ampatzi, E., Andargie, M. S., Andersen, R. K., Azar, E., Barthelmes, V. M., Berger, C., Bourikas, L., Carlucci, S., Chinazzo, G., Edappilly, L. P., Favero, M., Gauthier, S., Jamrozik, A., Kane, M., Mahdavi, A., Piselli, C., Pisello, A. L., Roetzel, A., … Zhang, S. (2020). Review of multi-domain approaches to indoor environmental perception and behaviour. *Building and Environment*, *176*. https://doi.org/10.1016/j.buildenv.2020.106804

Vargas, J. D., Autretto, G., Gentile, V., Shtrepi, L., & Fantucci, S. (2023). *3D Printed Architectural Components to Enhance Indoor Environmental Quality*.

Vincent, J. F. V. (2001). *Stealing Ideas From Nature*.

Zohdi, N., & Yang, R. C. (2021). Material anisotropy in additively manufactured polymers and polymer composites: A review. In *Polymers* (Vol. 13, Issue 19). MDPI. https://doi.org/10.3390/polym13193368

Zu, K., Qin, M., Rode, C., & Libralato, M. (2020). Development of a moisture buffer value model (MBM) for indoor moisture prediction. *Applied Thermal Engineering*, *171*. https://doi.org/10.1016/j.applthermaleng.2020.115096